Draft version August 3, 2020
Typeset using LaTeX **twocolumn** style in AASTeX63

Possible Activity in 468861 (2013 LU28)

Lily A. Slemp,[1] Karen J. Meech,[2] Erica Bufanda,[2] Jan T. Kleyna,[2] James Bauer,[3] Robert Weryk,[2] Larry Denneau,[2] Olivier Hainaut,[4] Jacqueline V. Keane,[2] and Richard Wainscoat[2]

[1] *Trinity University, 1 Stadium Drive, San Antonio, TX 78212 USA*
[2] *Institute for Astronomy, 2680 Woodlawn Drive, Honolulu, HI 96822 USA*
[3] *University of Maryland, Dept. of Astronomy, College Park, MD 20742-2421 USA*
[4] *European Southern Observatory, Karl-Schwarzschild-Strasse 2, D-85748 Garching bei München, Germany*

(Received TBD; Revised TBD; Accepted TBD)

Submitted to ApJ Letters

ABSTRACT

Manx comets are objects on long period (LP) comet orbits that lack the typical outgassing from near surface ices of LP comets as they approach perihelion. These comets are of particular interest because they may help constrain solar system formation models. The Manx 2013 LU28 was discovered as an inactive asteroidal object on 2013 June 8 at a heliocentric distance of 21.8 au. At such a large distance from perihelion this allows for the unique chance to observe this Manx comet over a long period of time on its approach to the sun, and to monitor its activity. We present an analysis of the activity and physical properties of Manx candidate 2013 LU28. Images and photometric data were obtained of 2013 LU28 from multiple telescopes from pre-discovery data in 2010 until the present. These data were used to determine the color of our target and its spectral reflectivity, as well as to determine if any activity was present. Preliminary results suggest that its spectral reflectivity is consistent with typical organic rich comet surfaces with colors of g'-r' = 0.97±0.02, r'-i' = 0.43±0.02 and r'-z' = 0.65±0.03, corresponding to a spectral reflectivity slope of $1.688 \pm xxx\%$/100nm [add error]. There is no obvious indication of activity in deep stacked images, however, comparison with the heliocentric light curve suggests possible outbursts near $r \sim$17 au. This is consistent with subsurface CO or CO_2 outgassing. The modeling of the bare nucleus with the heliocentric light curve gives an estimated nucleus radius size of ∼55.7±0.3 km. We present predictions for 2013 LU28 that will be useful for planning observations with JWST and large ground-based facilities as it comes to perihelion in 2024.

Keywords: asteroids: individual (2013 LU28) — comets: general

1. INTRODUCTION

Object (468861) 2013 LU28 was discovered by the Mt. Lemmon Survey on 2013 June 8. It has a long-period (LP) comet orbit (a=187.099 au, e=0.953, i=125.35°, q=8.736 au, Q=365.463 au, P=2559.28 yr) and will reach perihelion on 2024 June 21. However, although the orbit of 2013 LU28 identified it as a LP comet, there has been no dust coma associated with comet activity that has been observed. This suggests that 2013 LU28 is a "Manx" comet – an object coming from the Oort cloud with a LP orbit that lacks the typical outgassing from near surface ices of a LP comet (Meech et al. 2016).

Manx comets are unique in the fact that they are objects on a long period comet orbit that show very little to no activity. In 1950, although Jan Oort (Oort 1950) did not include these inactive objects in his study and inference of the existence of the Oort Cloud, he proposed an idea of where these inactive LP objects could be coming from. He proposed that the"disappearances" of the bright, highly-active comets that were coming from the Oort cloud could be due to the loss of a layer of volatile frosting, or a highly reactive outer layer that is lost once these comets first approach perihelion. Later, Levison proposed that these missing comets that Oort observed disrupted, and that there shouldn't be inactive objects

Corresponding author: Karen J. Meech
meech@ifa.hawaii.edu

on these LP orbits (Levison et al. 2002). Alternatively, there is a more recent possibility in that some of these objects coming from the Oort cloud may never have had significant volatiles. The "Manx comets" may represent objects that formed in the inner solar system and never had much ice. Manx comets, if they formed inside of the snowline of the early solar system before they were ejected outwards to the Oort cloud, could show evidence of this chemistry (Meech & Raymond 2020).

Several models can account for much of the formation and current architecture of our solar system, including the Nice model (Gomes et al. 2005), the Grand Tack model (Walsh et al. 2011), and the model by Raymond and Izidoro (Raymond & Izidoro 2017). In the Grand Tack model, the fully grown gas giants migrate from the location of their initial formation into the inner solar system, before moving out to their final orbital distances around the sun. This would lead to a scattering of volatile-rich (C-type) bodies from past the snowline inwards and volatile-poor (S-type) rocky bodies within the snowline outwards towards the Kuiper belt and Oort cloud (Walsh et al. 2012). The Nice model then describes the instability and migration of the orbits of Jupiter and Saturn that lead to a major restructuring of the orbits of the gas giants along with the smaller planetesimal bodies. This leads to further scattering of the volatile-rich (C-type) planetesimals that were out past the snow line in towards the inner solar system (Tsiganis 2015). In Raymond and Izidoro's model, this model describes how small planetesimal bodies can be scattered throughout the solar system even without the massive migration of the giant planets. Each of these models predicts a different fraction of Manxes out in the Oort cloud.

The patterns and amount of inner solar system material that is found in the Oort cloud from scattering will differentiate between the predictions of the various solar system models (Meech et al. 2016). The spectral reflectivity of inner solar system material is distinctly different from organic rich outer solar system material, which is red. Inner solar system material has a shallow 1 μm absorption feature from the presence of anhydrous minerals that cannot form in the presence of water. Along with interest in the spectra of the object, observing the activity of a dynamically old long period comet over a long duration of it's orbit can give essential insight into the distribution of volatiles in the solar system. Comets are often unable to be studied long before their perihelion date and characterization of CO and CO_2 sublimation for LPCs is difficult because water sublimation often takes over, lifting optically significant dust grains at heliocentric distances less than ∼6 au (Meech et al. 2003). Analyzing 2013 LU28 gives us a unique opportunity to search for CO and CO_2 sublimation.

In this paper, we will use data from multiple telescopes to determine the spectral reflectivity of 2013 LU28 to look for the surface features and absorption bands characteristic of minerals at 1 μm. We will also use the data to determine the approximate size of the nucleus and to constrain and characterize any detected activity, which we will investigate with a sublimation model.

2. OBSERVATIONS AND DATA REDUCTION

We obtained images of 2013 LU28 using the following facilities: Canada-France-Hawaii Telescope (CFHT) and Gemini-North on Mauna Kea, Hawai'i; Himalayan Chandra Telescope (HCT) on Mt. Saraswati, Hanle, India; Pan-STARRS (Magnier et al. (2016a); Denneau et al. (2013)) and ATLAS on Haleakelā, Hawai'i (Tonry et al. 2018a), and NEOWISE surveys (Mainzer et al. 2011). The particulars of the facilities are shown in Table 1. Unless otherwise noted, we used our own pipeline software for flattening. To photometrically calibrate the data we calculated a photometric zero point for each image using the Pan-STARRS, SDSS and Gaia2 catalogs and published color corrections to translate photometric bands (Magnier et al. 2016b; Chambers et al. 2016). The information from the image headers was used to download orbital elements from the Minor Planet Center and the computed object location was used to determine which object in the frame corresponded to the target. Terapix tools (SExtractor (Bertin & Arnouts 1996)) were used to produce multi-aperture and automatic aperture target photometry for several of the data sets. A full description of the pipeline is given in Meech et al. (2017).

Table 1. Observations

Telescope	Detector	Gain	RN	″/pix	Nts	# †
Gemini	GMOS	1.65	3.98	0.1614	14	41
CFHT	Megacam	1.634	3.00	0.187	22	68
HCT	HFOSC1	0.254	5.800	0.296	6	92
HCT	HFOSC2	0.254	5.800	0.180	8	71
PS1	GPC1	1.256	7.462	0.260	62	190
ATLAS	STA-1600	2.0	11.0	1.86	33	153

NOTE—†Number of CCD images

All of the photometry reported in this paper is in the SDSS system (Fukugita et al. 1996). The transformations between photometric systems depends on the color of the object. We used Gemini measurements obtained

on 2017 April 4 yielding $(g'\text{-}r') = 0.97\pm0.02$, $(r'\text{-}i') = 0.43\pm0.02$ and $(r'\text{-}z') = 0.65\pm0.03$ for all the subsequent filter system transformations.

To convert the R (Cousins) system magnitudes to the SDSS-band r-band shown in Table 3, we used the transformations of Lupton (2005)

$$r' = R + 0.1837(r - i) + 0.0971 \quad (1)$$

The transformations from the PS1 filters to the SDSS band r are given by Tonry et al. (2012).

$$r' = g_{P1} + 0.011 - 0.875(g' - r') + 0.015(g' - r')^2, \quad \sigma_{r'} = (0.006^2 + \sigma_{gp1}^2)^{0.5} \quad (2)$$

$$r' = r_{P1} - 0.001 + 0.006(g' - r') + 0.002(g' - r')^2, \quad \sigma_{r'} = (0.002^2 + \sigma_{rp1}^2)^{0.5} \quad (3)$$

$$r' = i_{P1} + (r' - i') - 0.004 + 0.014(g' - r') - 0.001(g' - r')^2, \sigma_{r'} = (0.003^2 + \sigma_{ip1}^2)^{0.5} \quad (4)$$

$$r' = z_{P1} + (r' - z') + 0.013 - 0.040(g' - r') + 0.001(g' - r')^2 \sigma_{r'} = (0.009^2 + \sigma_{zp1}^2)^{0.5} \quad (5)$$

$$r' = w_{P1} - 0.018 - 0.118(g' - r') + 0.091(g' - r')^2 \quad \sigma_{r'} = (0.012^2 + \sigma_{wp1}^2)^{0.5} \quad (6)$$

The transformations from the ATLAS filter system described are given in Tonry et al. (2018b). Write in errors

$$r' = 0.35(o + 0.678) + 0.65o \quad (7)$$

$$r' = 0.35c + 0.65(c - 0.678) \quad (8)$$

The transformations from the Gaia filter system are given in Jordi et al. (2010)

$$r' = G - (g' - r') + 0.0940 + 0.5310(g' - i') + 0.0974(g' - i')^2 \quad (9)$$

$$\sigma_g = (\sigma_G^2 + 0.09^2)^{0.5} \quad (10)$$

2.1. *CFHT*

We obtained images using the CFHT MegaCam wide-field imager, an array of forty 2048×4612 pixel CCDs with a plate scale of 0.″187 per pixel and a 1.1 square degree FOV. The data were obtained through SDSS filters using queue observing and were processed to remove the instrumental signature through the Elixir pipeline (Magnier & Cuillandre 2004). We have data obtained during 22 separate nights, as shown in Table 3.

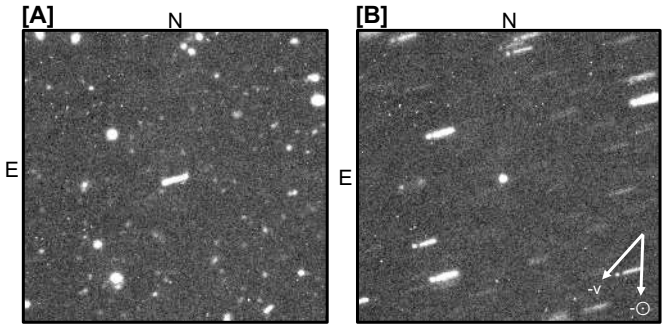

Figure 1. Stacked CFHT data of the object on 2018 May 6 for a total exposure time of 1921 seconds. Image A is stacked on the stars, while image B is stacked on 2013 LU28 at non-sidereal rates. Fix labels and crop sides slightly more (square).

2.2. *Gemini North*

We have 8 queue-scheduled observations of 2013 LU28 from April 2017 to February 2020. These were collected from the Gemini-North telescope using GMOS with 2 × 2 binning. Our custom observing planning tool was used to schedule observations to avoid contamination from field stars and galaxies and nearby bright sources. All raw images were reduced with Gemini's new python-based data reduction platform, DRAGONS (Labrie et al. 2019). We cropped the images to remove traces of air bubbles and other artifacts, and extracted the central chip on nights where the outer chips were non-photometric due to vignetting. We measured the photometry for these images using IRAF with a 2″ radius aperture. These images were also used to find the spectral reflectivity of 2013 LU28 over four different filters.

Lily - you need to add the new Gemini data to the plot and table.

2.3. *Himalayan Chandra Telescope*

Images were obtained from the 2.01 m Himalayan Chandra Telescope (HCT) at Mt. Saraswati, Hanle India. We used the Himalaya Faint Object Specropraph and Camera (HFOSC) and the new 4k×4k e2V CCD with the Bessell/Cousins filter system to obtain data on the dates shown in Table 3.

2.4. *Pan-STARRS1*

Pan-STARRS1 (PS1) is a 1.8 m wide-field survey telescope with a 3.2°×3.2° 1.4 gigapixel camera (GPC1). The detector is composed of 60 orthogonal transfer arrays, each with 64 590×598 pixel CCDs (Kaiser et al. 2002). A search for pre-discovery observations in the PS1 images taken between 2010 to 2020 produced images for 2013 LU28 during 62 separate nights. Photom-

etry was initially measured with an automatic 5″ radius aperture for all of the images, resulting in relatively large errors with the measurements and a wide spread of observed magnitudes within small amount of time. In order to obtain better magnitude measurements of these images, photometry was done using IRAF with a 1″ radius aperture, with corrections applied using the curve of growth of a bright, unsaturated star. All images were examined for quality and averaged over the same night.

Any individual photometric measurements were made using IRAF. In many of the early PanSTARRS images when 2013 LU28 was beyond r ∼17 au, the object was near the limit of detection. We used small apertures to minimize the sky noise, then used the curve of growth on a bright unsaturated star to correct for the amount of light lost. This process was done for all of the filters available for a given date. For the magnitude measurements used for the spectral reflectivity a 1″ radius aperture was used to measure the magnitude in order to minimize errors. The same aperture size was used for all images for the sublimation model.

2.5. *NEOWISE*

The NEOWISE survey (Mainzer et al. 2014) observed the position of 2013 LU28 during TBD visits. The first was for TBD exposures between date/time UT and date/time UT, with a mid-frame observing time of TBD UT. The $W2$ band encompasses both the CO 1-0 and CO_2 ν_3 emission bands. These visits showed no significant detections, and using the techniques described in Bauer et al. (2015) yielded TBD-σ upper limit for the nucleus size of TBD km.

2.6. *ATLAS*

Images were obtained by ATLAS in Hawaii consisting of two 0.5 m telescopes in Hawaii, using a STA-1600 detector with a 10.5×10.5k CCD array as shown in Table 1. The automatic measurements of the magnitude of 2013 LU28 were found with an image subtraction pipeline. All of the images were examined and averaged over the same night.

All of the photometry is shown in Table 3 and the data are plotted in Fig. 3.

3. ANALYSIS

3.1. *Spectral Reflectivity*

We used IRAF to do photometric measurements of the Gemini images and developed the curve of growth to get the optimal aperture size for spectral reflectivity. Magnitudes with a 1″ radius aperture were also obtained for the sublimation modeling (See §3.3). Once the optimal aperture size was determined for each image, we used the magnitude measurements to compute the spectral reflectivity of 2013 LU28. We converted the magnitude measurements and their uncertainties to a relative spectral reflectivity using

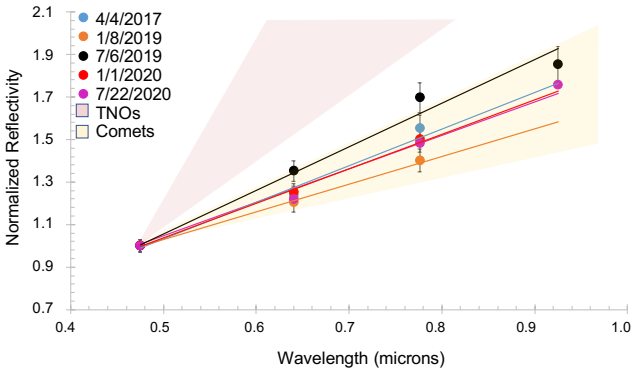

Figure 2. The spectral reflectivity of 2013 LU28 in the g, r, i, and z bands normalized to 1.0 in g and spanning from 2017 to 2020. Positive slope indicates a red color in the surface material. The color is consistent with comet surface colors and does not resemble the red-ultra red surfaces of organic rich TNOs.

$$R_\lambda = \frac{10^{-0.4(m_\lambda - m_{\lambda\odot})}}{10^{-0.4(m_o - m_{o\odot})}} \tag{11}$$

$$\sigma_R = 0.921R\left[\sigma_{m_\lambda}{}^2 + \sigma_{m_\lambda\odot}{}^2 + \sigma_{m_o^2} + \sigma_{m_o\odot}{}^2\right]^{0.5} \tag{12}$$

The term m_λ is the magnitude in a specific filter λ, σ_λ is the uncertainty on m_λ, m_o is the reference bandpass that we normalize to, and $m_\odot$ is the absolute magnitude of the sun. In the SDSS System the solar colors[1] are given by $g_\odot = 5.12\pm0.02$, $r_\odot = 4.68\pm0.03$, $i_\odot = 4.57\pm0.04$, $z_\odot = 4.54\pm0.04$. 2013 LU28's surface color is similar to cometary colors measured from in-situ space missions (9P, 103P and 67P) and not like TNOs as determined from BVRI photometry (see Fig. 2).

The spectral reflectivity gradients for 2013 LU28 expressed in %/100 nm are calculated from

$$S'(\%/100nm) = (\frac{20}{\Delta\lambda})[\frac{10^{0.4\Delta m} - 1}{10^{0.4\Delta m} + 1}] \tag{13}$$

where Δm is the comet color minus the solar color and $\Delta\lambda$ (μm) is the difference in the effective wavelengths of the bandpasses. The average for 2013 LU28 is S' = xxx %/100 nm.

3.2. *Nucleus Size*

[1] http://classic.sdss.org/dr4/algorithms/sdssUBVRITransform.html

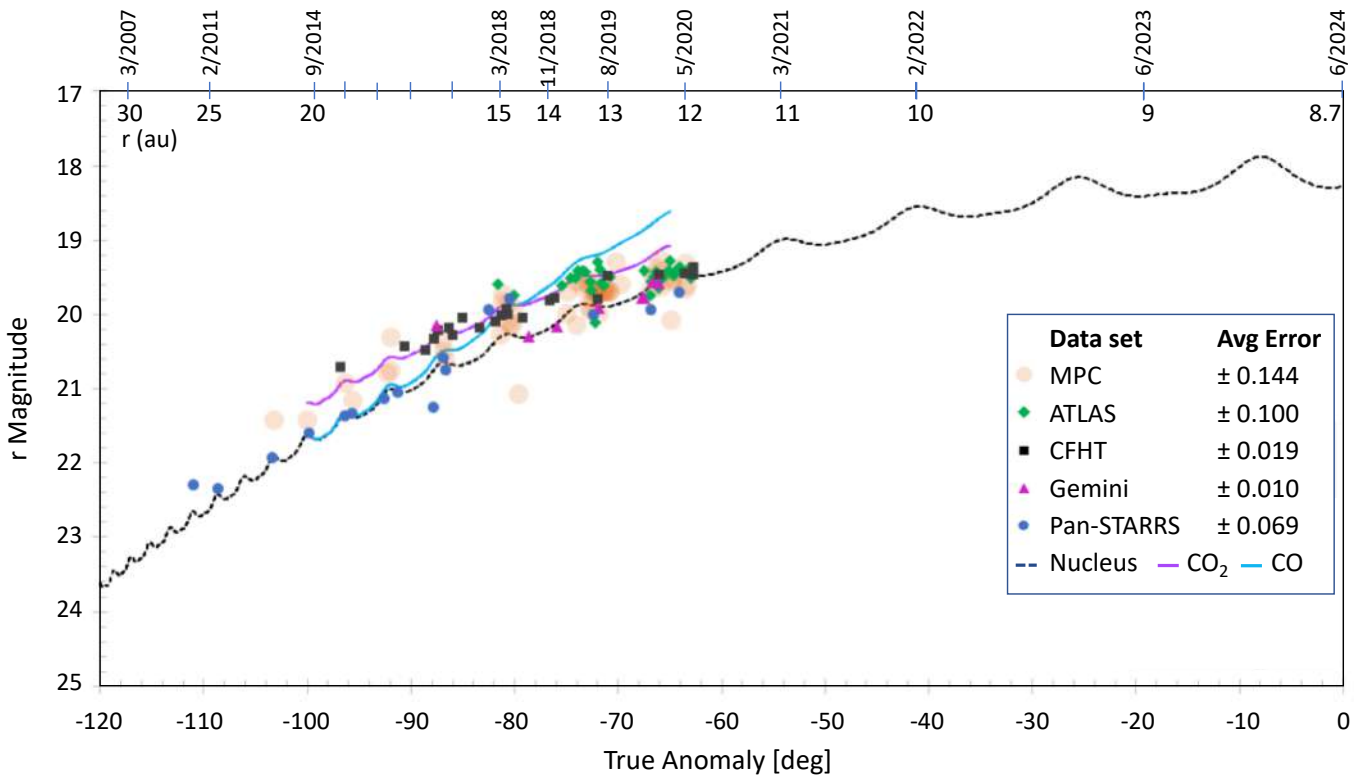

Figure 3. The asteroidal light curve (plotted for a nucleus radius ∼55.7 km, $p_r = 0.04$) suggests that there may have been activity near -90 < TA (deg) < -70 (r ∼17.2-13.1 au) between June 2016 to August 2018.

Exploration of all of the NEOWISE data showed no detection of 2013 LU28. Deep stacks were made to obtain upper limits for the nucleus radius. (He promised to get this to us after the holiday break - KJM I'll ping him again. If his nucleus upper limit is smaller than what we see, this will be interesting because it could give us some information about albedo.)!

3.3. *Sublimation Models*

We used a surface ice sublimation model (Meech et al. 1986) to investigate the activity for comet 2013 LU28. The model computes the amount of gas sublimating from an icy surface exposed to solar heating, as described in detail in Meech et al. (2017). The total brightness within a fixed aperture combines radiation scattered from both the nucleus and the dust dragged from the nucleus in the escaping gas flow, assuming a dust to gas mass ratio of 1. This type of model can distinguish between H_2O, CO, and CO_2 driven activity. The model free parameters include: nucleus radius, albedo, emissivity, nucleus density, dust properties, and fractional active area. When there is information about some of the parameters, it is possible to constrain many of the others.

Because 2013 LU28 is a relatively unstudied object, none of the model parameters are constrained. However, based on typical values for other comets seen in-situ and from the ground (Meech et al. 2017), we assumed the following: nucleus albedo, p_v=0.04, emissivity, ϵ=0.9, nucleus phase function, β=0.04 mag deg^{-1}, coma phase function, β_c=0.03 mag deg^{-1}, nucleus density, ρ_N=400 kg m^{-3}, and an average dust size of 5 μm. With steep power law size distributions for grains ranging in size between 0.1μm-mm, the small particles dominate (Kolokolova et al. 2004). With knowledge of the nucleus size, the fractional active area can be fit.

We ran a suite of models with a range of nucleus sizes, using least squares fitting to minimize the chi-squared residuals and found that for a radius $R_N \sim 55.7 \pm 0.3$ km the model brightness for the nucleus approached that of the photometry assuming an albedo p_v=0.04. The data between -90° < TA < -70° (r ∼17.2-13.1 au) is brighter than can be fit by an asteroidal brightening law and was excluded from this fitting. Individual images showed no evidence for any dust coma.

Assuming that the excess brightness is due to activity, we ran some sublimation models for CO and CO_2 as discussed in §3.4. We found that a circular area of radius ∼1300 m for CO_2 surface ice sublimation or radius ∼240 m of CO ice would produce a brightening of the comet to a degree that matches the data seen from -90° < TA <

-70°, which is too far out from the sun for any water-ice sublimation.

3.4. *Dust Production Limits from Image Profile Analysis*

Given that in §3.3 we are demonstrating that 2013 LU28 must be active, why don't we see any dust? In order to search for dust, we made deep stacks of images. The central x and y pixels of the object were located in 17 nights of CFHT images spanning from 2016 September 16 to 2019 August 13. Individual images were shifted accordingly to place the object on the same pixel in every image. Deep sky flats were made in order to correct for any non-uniformities in the sky background by dividing all images by their exposure time and subtracting out the background counts. The images were then median combined to remove any traces of the stars outside of the object itself. The resulting image shows no obvious indication of a coma around the object, as shown in Fig. 4.

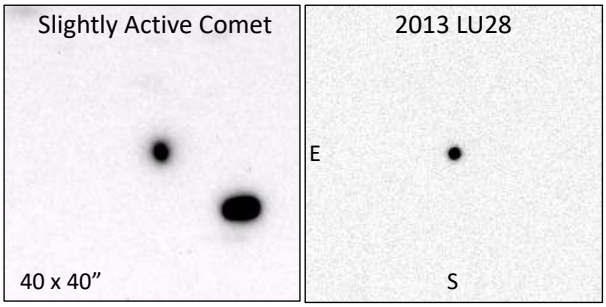

Figure 4. [A] A slightly active comparison object, which shows a slight dust coma around the nucleus at a distance of $r = 11.8$ au. [B] A deep stack of 2013 LU28 from 17 nights of images from CFHT Megacam that shows no obvious coma. The FOV is $40\times40''$, with a total exposure time of 40 minutes in the r' band.

To calculate an approximate upper limit on the dust production and activity for 2013 LU28 given its approximate nucleus size and brightness, we compared the average normalized surface brightness profiles of reference field stars to that of our object. The subtraction of the normalized stellar profile fluxes from those of an untrailed object with no apparent coma should yield a value of zero with an associated error. The 3σ of this error can be used as the limiting possible maximum flux contributed from scattered coma light that went undetected. This flux is given by (Meech & Weaver 1996):

$$F = \frac{S_\odot \pi {a_{gr}}^2 p_v Q \phi}{2 r^2 \Delta^2 v_{gr}} \quad (14)$$

where $S_\odot$ is the solar flux through the bandpass [W m^{-2}], a_{gr} [m] the grain radius, p_v the grain albedo, Q [kg s^{-1}] the dust production rate, ϕ the projected size of the aperture [m], v_{gr} [m s^{-1}] the grain velocity, and r is in au and Δ in m. If an empirical Bobrovnikoff relation for the terminal grain velocities is assumed (Bobrovnikoff 1954), $v_{gr} = v_{bob} = 600\ r^{-0.5}$, and $\phi = \Delta\ \phi^{'}\ /\ 206265$ where $\phi^{'}$ is the angular size of the aperture ($''$), then for a given observed flux, the dust production will vary as

$$Q \propto r^{1.5} \Delta \quad (15)$$

The most sensitive limits will be made when the object is observed at the smallest heliocentric distance. Further, because the sky noise dominates the errors in the surface brightness at larger apertures, the most sensitive limits on the dust will be made close to the nucleus, just outside the seeing disk.

To produce the normalized surface brightness profiles of both the reference stars and the object, we super-flattened and stacked 8 images from CFHT Megacam on 2018 May 16. The photometry of eight reference stars that were at least 60 pixels or $11''$ from other objects was done in an image stacked on the stars. Photometry of the object was done in an imaged stacked at non-sidereal rates. We calculated the surface brightness of the stars and object from the flux and normalized them to the magnitude brightness of the comet. The normalized surface brightness of the two stars were averaged, then a 3σ upper limit on the possible dust production was found at increasing aperture sizes.

Given that the seeing for these images averaged at approximately $1\farcs0$, the dust production estimates just outside of this aperture places the limit of 1.02 kg s^{-1} for 1 μm grains coming from the surface at $r = 14.7$ au.

We ran sublimation models for various volatiles to see how much ice could be sublimating and removing dust at this level. We found that a circular area of radius ~130 m for CO_2 surface ice sublimation or radius ~22 m of CO ice would produce this limiting amount of dust. At this distance from the Sun, the temperatures are too low for any water ice sublimation. The results are shown in Table 2 and in Fig. 5.

4. DISCUSSION

Given the apparent activity of 2013 LU28 from -90° < TA < -70 (r ~17.2-13.1 au), it is possible that there was an outburst of activity from deeply buried CO or CO_2 ice beneath the surface. With an eccentricity of 0.953, this object is not dynamically new, having been heated on many perihelion passages. During sublimation, gases both escape into space and migrate into the interior of the comet. The gas that migrates inwards encounters colder temperatures, and freezes in irregular layers of solid ice (Sarid et al. 2005). As heat from the sun pen-

Table 2. Outgassing from Dust Production Limits

TA [deg]	r [au]	Gas	f_{active}	Rad† [m]	Q§ [kg/s]	T [K]	a_{crit}‡ [μ m]	v_{dust} [m/s]
-80.9	14.7	CO	3.84E-8	22	1.0E-2	34	230	xxx
-80.9	14.7	CO_2	1.34E-6	130	1.1E-2	86	10	xxx
-90 to -80	17.1-14.7	CO	4.50E-6	240	1.1	33	200	xxx
-90 to -80	17.1-14.7	CO_2	1.30E-4	1300	1.5	84	5	xxx

†Radius of equivalent circular patch of ice sublimating to match the dust production limits. §Model dust production rate assuming 10 μm grains; ‡Maximum dust grain size that can be lifted in the gas flow.

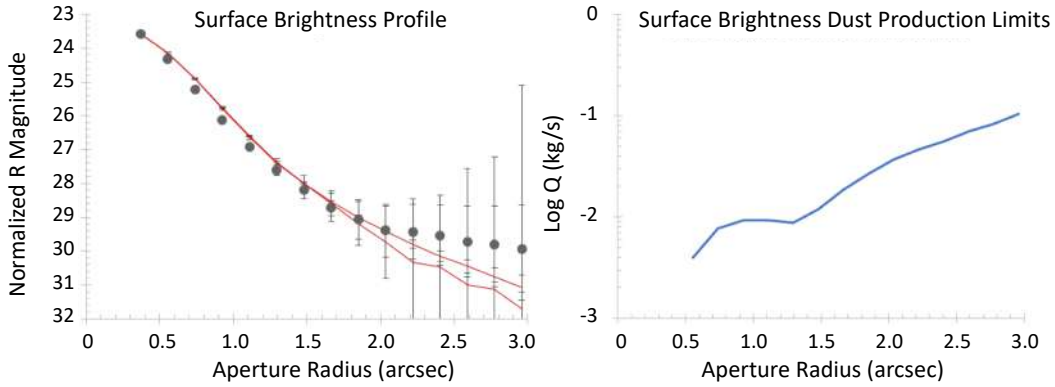

Figure 5. [A] The surface brightness profile of 2013 LU28 from 2018 May 16 (TA = -80.7°) compared to field stars shows that there is no scattered light contributed from any dust coma. [B] Using Eqn. 15, the difference in profiles is converted to a maximum dust production rate that can remain undetected.

etrates the approaching comet, ice beneath the surface can begin to sublimate, building pressure until it breaks through the solid ice above. The escaping gas will lift dust grains from the surface, increasing the brightness of the object. The Deep Impact, EPOXI, and Rosetta missions showed that even at perihelion, there was very little ice on the comet's surface, however water ice was close to the surface (A'Hearn et al. 2012; Capaccioni et al. 2015).

In the regime where the temperatures are high enough that most of the the incident energy is going into sublimation, the very volatile ices will be lost from the surface and migrate to deeper layers. Because the comet nucleus is highly porous, processes that would normally be confined to the surface can occur at deeper layers – e.g. sublimation of ice condensed onto the pore walls. The gas flowing inward will result in a chemical differentiation in the nucleus with the most volatile species at lower depths. Between 17-20 au when 2013 LU28 may have been active, the surface is cold enough that CO_2 would be just beginning to sublimate. However, if there were significant surface CO_2 ice, then the brightness should have continued to increase to the present, but it has not. It is more likely that the activity is driven by sublimation from sub-surface CO ice.

In the case of 2013 LU28, the activity seen may be similar to the Centaur 95P/Chiron. 95P/Chiron was found to have a long slow outburst of activity beginning near 14 au and decreasing until ∼11 au (Meech & Belton 1990; Meech et al. 1997). The cause of this activity was determined to be crystallization of amorphous water ice (Prialnik et al. 1995). Many laboratory experiments have shown that sub-surface release of gas can result in lifting large (100's of microns and larger) grains from the surface (Kochan et al. 1998; Bar-Nun & Laufer 2003). There was very little evidence of the activity seen from the ground. Because of Chiron's large size (radius 95 km) the grains were being lifted from the surface on ballistic trajectories which were then perturbed by solar radiation pressure into a bound dust atmosphere (Meech & Belton 1990). Only some small grains escaped and were imaged from the ground at very low surface brightnesses. The bound atmosphere was imaged by HST in Meech et al. (1997).

In a typical comet, dust is lifted off of the surface of the comet by the flow of sublimating gas [cite Finson and Probstein 1968, Wallis 1982, Gombosi 1986, Kita-

mura 1986, 1987]. Once the dust reaches a few nuclear radii above the surface of the comet, the gas and small dust particles become dynamically decoupled [cite Ney and Merrill 1976, Giese 1980]. By this time, most of the optically observed dust has been accelerated near to the gas flow velocity, which is much greater than the typical nuclear escape velocity. Thus, the visible dust coma of a typical comet is dominated by scattering from dust particles that are on escape trajectories. Escape velocities are only possible, however, with dust particles that are small enough to be lifted from the surface and remain dynamically coupled to the gas until it reaches escape velocities. Any larger particles that manage to be lifted off of the surface by the gas remain on bound ballistic trajectories, following orbits that mostly remain with in the comet's Hill lobe before they collide back down with the surface (Meech & Belton 1990). The Hill lobe is where the gravitation forces from the comet remains greater than the gravitational force from the sun. The Hill lobe is given by

$$R_{Hill} = r[\frac{m}{3m_{\odot}}]^{1/3} \tag{16}$$

where R_{Hill} is the radius of the Hill lobe in km, r is the heliocentric distance in km, m_N is the mass of the nucleus in g, and $m_{\odot}$ is the mass of the sun. As these larger particles remain above the surface of the comet on their ballistic trajectories, they can be perturbed by radiation pressure and complete several orbits around the comet nucleus before colliding with the surface [cite Bishop and Chamberlain 1989]. The Hill radius for 2013 LU28 was found to be approximately 7.7″ in radius between r=20 to 14 au.

In a parallel approach, Bishop (**?**) introduced the concept of an "exopause" to describe the level in a planet's atmosphere where the acceleration due to radiation pressure exceeds that due to the gravitational attraction of the planet. Particles on trajectories which intersect the exopause are presumed to be so strongly affected by radiation pressure that they are effectively lost to space. The distance to the exopause is therefore a function of the heliocentric distance, and is given by

$$R_{exopause} = r[\frac{m_N}{m_{\odot}\beta}]^{1/2} \tag{17}$$

where β is the ratio of the forces due to the Sun's radiation and gravity is defined by **?**. For a typical comet at 1 au, $r_exopause$ $\sim 2.4\beta^{-1/2}$ km. For 1 cm particles that might be gravitationally bound in a typical comet, $r_exopause$ $\sim$300 km (i.e. the exopause is within a few nuclear radii of the surface for the optically important particles). In general, the exopause is found to fall within the gravitational Hill radius of the nucleus. It is this level that effectively defines the physical limits to the influence of nuclear gravity. **?** also discusses this concept of the exopause with respect to the hydrogen geocorona seen about the Earth. They note that atoms whose initial velocities would have placed them in the bound population (within the Earth's Roche lobe) could actually escape under the influence of Ly α radiation pressure (i.e. particles with orbits above the exopause can escape and form a geotail). The influence of such large bound particles on the visual brightness of the coma of a typical comet at 1 au is negligible since their total effective scattering area for sunlight is an extremely small fraction of that presented by the population of optically significant particles on escape trajectories. We calculated the exopause for 2013 LU28 to be approximately 0.11″ in radius, which is well within the seeing disc of the telescope.

Like Chiron, 2013 LU28 could have a bound "atmosphere" of larger dust particles. 2013 LU28 shows evidence of brightening beginning near 17 au and continuing until around 14 au. The brightening begins as pressure is relieved from sublimating gasses beneath the surface, exposing ice that begins sublimating and lifting dust off of the surface. The bright trend continues as the exposed ice continues to sublimate and larger dust grains remain close to the object nucleus within the typical seeing of ground-based telescopes. The brightening only dims back to the apparent brightness of the bare nucleus once the thermally exposed ice is gone and substantial dust no longer surrounds the nucleus (Meech & Belton 1990). Table 2 shows the critical grain size that can be lifted off the surface in the gas flow against the pull of gravity from the nucleus. When only small grains are able to be lifted off of the surface, then since the optical observations are most sensitive to scattered light at micron scales, we may not see much material.

To further include in the discussion . . .:

- This object is very large compared to other comets. SP comets are small with sizes peaking around 1-2 km radius. They are likely fragments of KBOs. But LPCs formed separately. How do they compare to KBOs?
- Do we want to do more sophisticated thermal models with Dina?

Acknowledgements LAS acknowledges support from the National Science Foundation (NSF) Research Experience for Undergraduate program at the Institute for Astronomy, University of Hawai'i at Mānoa, funded through NSF grant 6104374. KJM, JTK, and JVK acknowledge support through awards from the National Science Foundation AST1413736 and AST1617015.

Based also in part on observations obtained with MegaPrime/MegaCam, a joint project of CFHT and CEA/DAPNIA, at the Canada-France-Hawaii Telescope (CFHT) which is operated by the National Research Council (NRC) of Canada, the Institute National des Science de l'Univers of the Centre National de la Recherche Scientifique (CNRS) of France, and the University of Hawai'i.

Data were acquired using the PS1 System operated by the PS1 Science Consortium (PS1SC) and its member institutions. The Pan-STARRS1 Surveys (PS1) have been made possible by contributions from PS1SC member Institutions and NASA through Grant NNX08AR22G, the NSF under Grant No. AST-123886, the Univ. of MD, and Eotvos Lorand Univ.

We thank the staff of IAO, Hanle and CREST, Hosakote, that made these observations possible. IAO and CREST are operated by the Indian Institute for Astrophysics, Bangalore.

Table 3. Observing Geometry and Photometry - NOTE: STILL UPDATING

UTDate	JD[a]	r^b	Δ^b	α^b	TA[c]	Filt	# Images	mag$\pm\sigma$[d]	$r_{mag}\pm\sigma$[e]	Color/Comment
Gemini North, GMOS - DONE										
2017/04/04	7848.11154	16.362	15.799	2.947	-87.589	g	1	21.115±0.019		(g-r) = 0.966±0.023
2017/04/04	7848.11242	16.362	15.799	2.947	-87.589	r	1	20.149±0.013	20.149±0.013	
2017/04/04	7848.11327	16.362	15.799	2.947	-87.589	i	1	19.717±0.015		(r-i) = 0.432±0.020
2018/08/31	8361.77467	14.343	14.739	3.661	-78.644	g	2	20.889±0.015		(g-r) = 0.966±0.023
2018/08/31	8361.77556	14.343	14.739	3.661	-78.644	r	1	20.260±0.020	20.260±0.015	
2018/08/31	8361.77642	14.343	14.739	3.661	-78.644	i	1	20.276±0.015		(r-i) = 0.432±0.020
2019/01/08	8492.09971	13.839	13.974	4.012	-75.955	g	2	20.804±0.010		(g-r) = 0.966±0.023
2019/01/08	8492.10076	13.839	13.974	4.012	-75.955	r	1	20.164±0.010	20.164±0.010	
2019/01/08	8492.10175	13.839	13.974	4.012	-75.955	i	1	19.947±0.010		(r-i) = 0.432±0.020
2019/07/06	8670.79726	13.158	13.120	4.434	-71.926	g	1	20.758±0.018		(g-r) = 0.966±0.023
2019/07/06	8670.79817	13.158	13.120	4.434	-71.926	z	1	19.504±0.024		(r-z) = 0.645±0.028
2019/07/06	8670.80229	13.158	13.120	4.434	-71.926	i	1	19.311±0.013		(r-i) = 0.432±0.020
2019/07/06	8670.80315	13.158	13.120	4.434	-71.926	r	1	19.926±0.013	19.926±0.013	
2019/12/20	8838.14905	12.534	12.729	4.373	-67.759	r	2	19.773±0.009		
2020/01/01	8850.09972	12.491	12.561	4.485	-67.446	g	3	20.468±0.008		(g-r) = 0.966±0.023
2020/01/01	8850.10060	12.491	12.561	4.485	-67.446	r	1	19.803±0.011	19.803±0.011	
2020/01/01	8850.10146	12.491	12.561	4.485	-67.446	i	1	19.551±0.013		(r-i) = 0.432±0.020
2020/01/31	8880.16852	12.381	12.142	4.467	-66.648	r	1	19.565±0.013	19.565±0.013	
2020/02/23	8903.15194	12.297	11.871	4.235	-66.030	r	4	19.583±0.005	19.583±0.005	
PanSTARRS1 - DONE (MOSTLY)										
2010/06/19	5366.96975	25.933	25.137	1.416	-110.957	r_{p1}	1	21.855±0.165	22.296±0.167	
2011/06/08	5720.99056	24.614	23.801	1.437	-108.644	i_{p1}	2	21.905±0.163	22.346±0.164	
2013/05/03	6416.07805	21.974	21.235	1.824	-103.490	r_{p1}	1	21.434±0.163	21.875±0.165	
2013/05/20	6433.03634	21.908	21.125	1.708	-103.351	r_{p1}	1	21.539±0.162	21.980±0.164	
2014/06/18	6826.99655	20.383	19.722	2.205	-99.865	i_{p1}	3	21.163±0.097	21.606±0.098	
2015/05/11	7154.01921	19.103	18.378	2.152	-96.534	i_{p1}	4	20.892±0.072	21.337±0.073	
2015/05/13	7156.04226	19.095	18.369	2.150	-96.512	i_{p1}	4	20.825±0.053	21.269±0.054	
2015/06/03	7177.04042	19.013	18.322	2.281	-96.281	i_{p1}	3	20.917±0.100	21.459±0.101	

Table 3 *continued*

Table 3 *(continued)*

UTDate	JD[a]	r[b]	Δ[b]	α[b]	TA[c]	Filt	# Images	mag$\pm\sigma$[d]	r$_{mag}\pm\sigma$[e]	Color/Comment
2015/06/04	7177.82387	19.010	18.322	2.290	-96.272	i$_{p1}$	3	20.932±0.080	21.373±0.081	
2015/06/11	7184.96372	18.981	18.329	2.390	-96.193	r$_{p1}$	4	20.986±0.046	21.428±0.047	
2015/07/26	7229.84083	18.805	18.566	3.028	-95.689	i$_{p1}$	2	20.974±0.097	21.416±0.098	
2015/07/27	7230.81742	18.801	18.574	3.036	-95.678	i$_{p1}$	4	20.839±0.064	21.280±0.065	
2015/08/01	7235.81376	18.781	18.615	3.069	-95.621	i$_{p1}$	4	20.933±0.084	21.375±0.085	
2015/08/03	7237.80746	18.774	18.631	3.079	-95.598	i$_{p1}$	2	20.865±0.064	21.307±0.066	
2016/02/27	7446.06549	17.952	17.771	3.123	-93.123	r$_{p1}$	2	20.786±0.076	21.227±0.077	
2016/03/20	7468.04393	17.865	17.441	2.925	-92.847	i$_{p1}$	4	20.753±0.049	21.195±0.051	
2016/03/30	7477.99304	17.826	17.311	2.792	-92.721	r$_{p1}$	4	20.731±0.046	21.172±0.048	
2016/04/21	7499.95882	17.739	17.086	2.515	-92.441	i$_{p1}$	7	20.551±0.042	20.992±0.043	
2016/05/16	7524.84557	17.641	16.952	2.453	-92.120	r$_{p1}$	1	20.636±0.111	21.077±0.113	
2016/06/02	7542.01490	17.573	16.937	2.624	-91.897	w$_{p1}$	4	19.607±0.027	19.792±0.030	
2016/06/27	7566.86143	17.475	17.014	3.011	-91.570	w$_{p1}$	4	19.419±0.020	19.600±0.023	
2016/07/22	7591.83082	17.376	17.175	3.304	-91.239	i$_{p1}$	4	20.612±0.054	21.054±0.055	
2017/03/21	7834.14645	16.417	15.955	3.126	-87.799	z$_{p1}$	1	20.627±0.114	21.247±0.120	
2017/05/18	7892.02040	16.188	15.555	2.850	-86.913	i$_{p1}$	2	20.144±0.046	20.585±0.488	
2017/05/26	7899.83840	16.157	15.553	2.941	-86.791	w$_{p1}$	4	19.179±0.014	19.361±0.018	
2017/06/01	7905.93715	16.133	15.560	3.026	-86.696	i$_{p1}$	2	20.311±0.053	20.752±0.055	
2017/08/13	7978.75996	15.845	15.982	3.617	-85.533	w$_{p1}$	2	19.060±0.023	19.244±0.029	
2018/02/09	8159.16937	15.135	15.020	3.724	-82.465	z$_{p1}$	1	19.312±0.087	19.932±0.094	
2018/05/31	8269.87155	14.701	14.209	3.515	-80.432	i$_{p1}$	4	19.347±0.023	19.788±0.026	
2018/06/10	8279.76456	14.662	14.243	3.666	-80.244	w$_{p1}$	4	18.837±0.012	19.020±0.017	
2018/06/24	8293.80598	14.608	14.312	3.855	-79.976	i$_{p1}$	2	xxx±xxx	xxx±xxx	
2019/04/06	8580.13057	13.502	12.933	3.573	-74.022	z$_{p1}$	1	xxx±xxx	xxx±xxx	
2019/04/20	8594.11549	13.448	12.876	3.597	-73.706	z$_{p1}$	1	xxx±xxx	xxx±xxx	
2019/04/25	8598.97691	13.430	12.866	3.631	-73.595	i$_{p1}$	1	xxx±xxx	xxx±xxx	
2019/05/25	8629.01065	13.316	12.894	4.027	-72.905	i$_{p1}$	4	xxx±xxx	xxx±xxx	
2019/06/09	8643.87116	13.259	12.957	4.238	-72.560	i$_{p1}$	4	xxx±xxx	xxx±xxx	
2019/06/10	8644.82675	13.256	12.962	4.250	-72.537	i$_{p1}$	4	xxx±xxx	xxx±xxx	
2019/06/13	8647.82517	13.244	12.978	4.285	-72.467	i$_{p1}$	4	xxx±xxx	xxx±xxx	
2019/06/14	8648.88736	13.240	12.984	4.296	-72.442	i$_{p1}$	2	xxx±xxx	xxx±xxx	

Table 3 *continued*

Table 3 *(continued)*

UTDate	JD[a]	r^b	Δ^b	α^b	TA[c]	Filt	# Images	mag±σ[d]	r_{mag}±σ[e]	Color/Comment
2019/06/20	8654.92317	13.218	13.019	4.355	-72.301	i_{p1}	4	xxx±xxx	xxx±xxx	
2019/07/05	8669.77386	13.162	13.113	4.432	-71.950	w_{p1}	4	xxx±xxx	xxx±xxx	
2019/07/10	8674.77501	13.143	13.146	4.435	-71.832	i_{p1}	4	xxx±xxx	xxx±xxx	
2019/07/13	8677.76839	13.131	13.166	4.430	-71.761	i_{p1}	8	xxx±xxx	xxx±xxx	
2020/01/18	8867.15562	12.428	12.319	4.527	-66.995	g_{p1}	1	20.342±0.092	19.525±0.095	
2020/01/18	8867.15834	12.428	12.319	4.527	-66.995	z_{p1}	1	19.489±0.046	20.109±0.059	
2020/01/29	8878.12716	12.388	12.169	4.481	-66.703	w_{p1}	2	xxx±xxx	xxx±xxx	
2020/01/29	8878.13951	12.388	12.169	4.481	-66.702	g_{p1}	1	20.479±0.148	19.662±0.150	
2020/01/29	8878.14225	12.388	12.169	4.481	-66.702	i_{p1}	1	19.373±0.053	19.814±0.058	
2020/01/29	8878.14302	12.388	12.169	4.481	-66.702	w_{p1}	2	xxx±xxx	xxx±xxx	
2020/04/12	8951.95145	12.121	11.587	4.103	-64.687	i_{p1}	4	xxx±xxx	xxx±xxx	
2020/04/12	8952.06400	12.121	11.587	4.104	-64.684	i_{p1}	4	19.688±0.038	20.127±0.048	
2020/04/30	8969.91286	12.057	11.597	4.345	-64.182	i_{p1}	4	xxx±xxx	xxx±xxx	
2020/05/01	8970.88104	12.053	11.599	4.360	-64.155	i_{p1}	4	19.128±0.016	19.573±0.020	
2020/05/04	8973.86040	12.043	11.606	4.408	-64.071	i_{p1}	4	xxx±xxx	xxx±xxx	
2020/05/09	8978.98528	12.024	11.622	4.490	-63.926	i_{p1}	4	19.154±0.017	19.603±0.020	
2020/05/11	8980.88875	12.017	11.629	4.521	-63.871	i_{p1}	4	19.103±0.012	19.547±0.017	
2020/05/31	9000.88198	11.946	11.727	4.794	-63.299	i_{p1}	4	xxx±xxx	xxx±xxx	
CFHT Megacam - DONE										
2015/04/23	7135.99314	19.174	18.505	2.285	-96.7291	r	1	20.928±0.043	20.928±0.043	
2015/04/23	7135.99732	19.174	18.505	2.285	-96.7291	g	1	21.485±0.028		(g-r) = 0.966±0.023
2015/04/23	7136.00158	19.174	18.505	2.285	-96.7291	i	1	19.941±0.042		(r-i) = 0.432±0.020
2015/04/23	7136.00585	19.174	18.505	2.285	-96.7290	z	1	xxx±xxx		(r-z) = 0.645±0.028
2016/09/05	7636.72723	17.198	17.518	3.159	-90.6314	r	1	20.429±0.053	20.429±0.053	
2017/01/26	7780.14268	16.631	16.761	3.348	-88.6001	r	2	20.481±0.031	20.481±0.031	
2017/03/29	7842.11299	16.385	15.862	3.023	-87.6794	r	4	20.328±0.019	20.328±0.019	
2017/04/21	7865.06951	16.295	15.657	2.789	-87.3300	g	2	20.974±0.040		(g-r) = 0.966±0.023
2017/04/21	7865.07289	16.295	15.657	2.789	-87.3299	r	2	20.262±0.029	20.262±0.029	
2017/06/24	7928.78021	16.043	15.640	3.376	-86.3355	r	2	20.186±0.023	20.186±0.023	
2017/07/16	7950.82653	15.956	15.777	3.615	-85.9841	r	2	20.282±0.027	20.282±0.027	
2017/09/18	8014.71884	15.703	16.189	3.164	-84.9449	r	2	20.053±0.029	20.053±0.029	

Table 3 *continued*

Table 3 *(continued)*

UTDate	JD[a]	r^b	Δ^b	α^b	TA[c]	Filt	# Images	mag±σ[d]	r_{mag}±σ[e]	Color/Comment
2017/12/23	8111.15059	15.324	15.727	3.308	-83.3112	r	2	20.188±0.015	20.188±0.015	
2018/03/19	8197.10346	14.986	14.510	3.400	-81.7814	r	2	20.105±0.010	20.105±0.010	
2018/04/23	8231.97991	14.849	14.237	3.143	-81.1413	r	2	20.023±0.012	20.023±0.012	
2018/05/16	8254.99660	14.759	14.188	3.304	-80.7121	r	8	19.931±0.007	19.931±0.007	
2018/05/22	8260.78012	14.737	14.192	3.381	-80.6033	r	2	19.999±0.015	19.999±0.015	
2018/08/07	8337.80621	14.436	14.604	3.950	-79.1194	g	3	20.794±0.014		(g-r) = 0.966±0.023
2018/08/07	8337.81287	14.436	14.604	3.950	-79.1193	r	3	20.085±0.013	20.085±0.013	
2018/12/09	8462.14742	13.954	14.378	3.594	-76.5891	r	2	19.811±0.016	19.811±0.016	
2019/01/02	8486.16188	13.862	14.059	3.952	-76.0813	r	2	19.781±0.017	19.781±0.017	
2019/07/05	8669.80958	13.161	13.113	4.432	-71.9495	r	2	19.795±0.014	19.795±0.014	
2019/08/13	8708.77304	13.015	13.353	4.156	-71.0162	r	3	19.483±0.018	19.483±0.018	
2020/02/26	8906.11682	12.286	11.841	4.201	-65.9489	r	2	19.471±0.012	19.471±0.012	
2020/05/26	8995.81445	11.964	11.698	4.737	-63.4451	r	2	19.459±0.016	19.459±0.016	
2020/06/20	9020.91035	11.876	11.855	4.910	-62.7191	r	4	19.365±0.013	19.365±0.013	
2020/06/23	9023.75812	11.866	11.874	4.910	-62.6363	r	6	19.463±0.023	19.463±0.023	
ATLAS - DONE										
2018/03/28	8206.12334	14.950	14.418	3.295	-81.617	o	1	19.350±0.155	19.587±0.155	
2018/06/03	8282.91890	14.650	14.256	3.713	-80.184	o	1	19.516±0.176	19.753±0.176	
2018/06/20	8289.93326	14.623	14.291	3.808	-80.050	o	1	19.490±0.179	19.727±0.179	
2019/02/03	8518.13172	13.739	13.593	4.087	-75.394	o	1	19.377±0.162	19.614±0.162	
2019/03/08	8551.14423	13.612	13.171	3.805	-74.670	o	1	19.420±0.191	19.657±0.191	
2019/03/12	8555.09218	13.597	13.130	3.761	-74.583	o	2	19.265±0.108	19.503±0.108	
2019/03/16	8559.11063	13.582	13.091	3.717	-74.493	o	2	19.213±0.102	19.450±0.103	
2019/03/28	8571.08783	13.536	12.991	3.613	-74.226	o	3	19.364±0.101	19.601±0.101	
2019/04/03	8577.10228	13.513	12.951	3.582	-74.091	c	3	19.765±0.114	19.324±0.114	
2019/04/09	8583.02949	13.491	12.918	3.569	-73.957	o	2	19.241±0.106	19.478±0.106	
2019/04/15	8589.06015	13.468	12.893	3.576	-73.820	o	1	18.994±0.145	19.231±0.145	
2019/05/03	8607.03137	13.399	12.858	3.713	-73.411	o	1	19.175±0.192	19.412±0.192	
2019/05/15	8618.93121	13.354	12.867	3.874	-73.138	o	1	19.185±0.167	19.422±0.167	
2019/05/31	8634.88597	13.293	12.915	4.115	-72.769	o	1	19.523±0.194	19.760±0.194	
2019/06/02	8636.86702	13.286	12.924	4.144	-72.723	c	1	19.732±0.159	19.291±0.159	

Table 3 *continued*

Table 3 *(continued)*

UTDate	JD[a]	r^b	Δ^b	α^b	TA[c]	Filt	# Images	mag±σ[d]	r_{mag}±σ[e]	Color/Comment
2019/06/08	8642.82498	13.263	12.952	4.225	-72.584	o	1	19.337±0.168	19.574±0.168	
2019/06/10	8644.89085	13.256	12.962	4.250	-72.536	o	2	19.463±0.104	19.700±0.104	
2019/06/22	8656.80450	13.211	13.030	4.370	-72.257	o	1	19.875±0.197	20.112±0.197	
2019/06/30	8664.80707	13.180	13.081	4.418	-72.068	c	3	19.734±0.081	19.293±0.082	
2019/07/04	8668.77250	13.165	13.107	4.430	-71.974	c	1	19.750±0.160	19.309±0.160	
2019/07/11	8675.84092	13.139	13.153	4.434	-71.806	o	1	19.158±0.189	19.395±0.189	
2019/07/20	8684.79832	13.105	13.212	4.403	-71.593	o	1	19.346±0.146	19.583±0.146	
2019/07/26	8690.80014	13.082	13.251	4.362	-71.449	o	1	19.368±0.168	19.605±0.168	
2019/08/21	8716.76172	12.985	13.389	4.035	-70.822	o	1	19.261±0.154	19.498±0.154	
2019/12/29	8847.07169	12.502	12.604	4.463	-67.525	o	2	19.180±0.077	19.419±0.077	
2020/01/20	8869.10660	12.421	12.292	4.523	-66.943	o	2	19.505±0.126	19.742±0.126	
2020/01/22	8871.04121	12.414	12.265	4.517	-66.891	o	3	19.412±0.087	19.649±0.087	
2020/01/24	8873.02690	12.407	12.238	4.509	-66.839	c	2	19.692±0.123	19.251±0.124	
2020/01/26	8875.12769	12.399	12.209	4.499	-66.783	o	5	19.425±0.063	19.662±0.064	
2020/01/28	8877.11851	12.392	12.183	4.488	-66.729	c	2	19.759±0.127	19.318±0.127	
2020/01/30	8879.04401	12.385	12.157	4.475	-66.678	o	6	19.256±0.053	19.493±0.054	
2020/02/03	8883.05983	12.370	12.105	4.444	-66.571	o	9	19.261±0.044	19.498±0.044	
2020/02/05	8885.11515	12.363	12.079	4.427	-66.515	c	3	19.884±0.097	19.443±0.097	
2020/02/15	8895.04792	12.327	11.959	4.326	-66.248	o	4	19.190±0.071	19.427±0.071	
2020/02/21	8901.12445	12.304	11.892	4.258	-66.084	c	1	19.471±0.175	19.030±0.175	
2020/02/23	8903.06204	12.297	11.872	4.236	-66.032	o	3	19.473±0.085	19.710±0.085	
2020/03/02	8911.04605	12.268	11.795	4.148	-65.815	o	4	19.248±0.075	19.485±0.075	
2020/03/06	8915.13027	12.254	11.760	4.108	-65.704	o	3	19.349±0.092	19.586±0.092	
2020/03/10	8919.07749	12.239	11.729	4.075	-65.596	o	1	18.979±0.184	19.216±0.184	
2020/03/24	8933.02719	12.189	11.643	4.013	-65.212	c	2	19.798±0.130	19.357±0.130	
2020/03/30	8939.09434	12.167	11.617	4.019	-65.045	o	3	19.186±0.065	19.424±0.065	
2020/04/03	8942.99023	12.153	11.605	4.035	-64.936	o	2	19.048±0.112	19.285±0.112	
2020/04/11	8950.97409	12.125	11.588	4.094	-64.714	o	2	19.328±0.111	19.566±0.111	
2020/04/15	8955.03900	12.110	11.585	4.137	-64.601	o	4	19.270±0.062	19.507±0.063	
2020/04/17	8956.97229	12.103	11.584	4.160	-64.546	c	1	19.272±0.122	18.831±0.122	
2020/04/21	8960.94256	12.089	11.585	4.211	-64.435	c	1	19.661±0.191	19.220±0.191	

Table 3 *continued*

Table 3 *(continued)*

UTDate	JD[a]	r[b]	Δ[b]	α[b]	TA[c]	Filt	# Images	mag$\pm\sigma$[d]	r$_{mag}\pm\sigma$[e]	Color/Comment
2020/04/23	8963.01632	12.081	11.586	4.240	-64.377	o	3	19.134±0.089	19.371±0.090	
2020/04/27	8966.94414	12.067	11.591	4.299	-64.266	o	3	19.225±0.078	19.462±0.078	
2020/05/01	8970.99049	12.053	11.599	4.362	-64.152	o	1	19.301±0.148	19.538±0.148	
2020/05/03	8972.93735	12.046	11.604	4.393	-64.097	o	2	19.050±0.128	19.287±0.129	
2020/05/05	8974.97580	12.039	11.609	4.426	-64.039	o	1	19.078±0.165	19.315±0.165	
2020/05/09	8978.92205	12.025	11.622	4.489	-63.927	o	2	19.072±0.118	19.309±0.118	
2020/05/11	8980.91374	12.017	11.629	4.521	-63.871	o	1	19.023±0.160	19.260±0.160	
2020/05/13	8982.88328	12.010	11.637	4.552	-63.815	o	4	19.344±0.066	19.581±0.067	
2020/05/15	8984.89536	12.003	11.645	4.583	-63.757	c	3	19.797±0.104	19.356±0.104	
2020/05/17	8986.92139	11.996	11.654	4.614	-63.700	o	4	19.130±0.057	19.367±0.058	
2020/05/19	8988.90129	11.989	11.663	4.643	-63.643	c	2	19.664±0.121	19.223±0.121	
2020/05/21	8990.86925	11.982	11.672	4.671	-63.587	o	2	19.321±0.093	19.558±0.093	
2020/05/23	8992.85900	11.975	11.682	4.699	-63.530	c	3	19.706±0.098	19.265±0.098	
2020/05/25	8994.87716	11.968	11.693	4.725	-63.472	o	2	19.286±0.093	19.523±0.093	
2020/05/29	8998.85153	11.954	11.715	4.772	-63.358	o	3	18.989±0.094	19.226±0.094	
2020/05/31	9000.85301	11.947	11.727	4.794	-63.300	o	2	19.238±0.087	19.475±0.088	
2020/06/02	9002.87159	11.939	11.739	4.814	-63.242	o	3	19.122±0.090	19.359±0.090	
2020/06/06	9006.83897	11.925	11.763	4.849	-63.128	o	1	18.915±0.136	19.152±0.136	
2020/06/10	9010.82630	11.911	11.788	4.876	-63.012	o	3	19.256±0.075	19.493±0.075	
2020/06/11	9011.82020	11.908	11.795	4.882	-62.983	c	1	19.927±0.186	19.486±0.186	
2020/06/14	9014.81867	11.897	11.814	4.896	-62.896	o	3	19.324±0.086	19.561±0.087	
2020/06/15	9015.82214	11.894	11.821	4.900	-62.867	c	2	19.869±0.120	19.428±0.120	
HCT HFOSC										
2014/03/20	6737.07683	22.221	22.202	2.569	-146.88	r$_{p1}$	2	20.67±0.30	20.67±0.30	
2014/09/08	6908.76850	21.364	21.430	2.692	-146.17	i$_{p1}$	4	20.60±0.05	20.77±0.05	

[a] Julian Date -2450000.0

[b] Heliocentric, geocentric distance (au) and phase angle (deg).

[c] True anomaly (deg), position along orbit, TA at perihelion=0°

[d] Magnitude and error through 5″ radius aperture.

[e] Magnitude and error converted to SDSS r as described in the text

REFERENCES

A'Hearn, M. F., Feaga, L. M., Keller, H. U., et al. 2012, ApJ, 758, 29

Bar-Nun, A., & Laufer, D. 2003, Icarus, 161, 157

Bauer, J. M., Stevenson, R., Kramer, E., et al. 2015, ApJ, 814, 85

Bertin, E., & Arnouts, S. 1996, A&AS, 117, 393

Bobrovnikoff, N. T. 1954, AJ, 59, 356

Capaccioni, F., Coradini, A., Filacchione, G., et al. 2015, Science, 347, aaa0628

Chambers, K. C., Magnier, E. A., Metcalfe, N., et al. 2016, ArXiv e-prints, arXiv:1612.05560

Denneau, L., Jedicke, R., Grav, T., et al. 2013, PASP, 125, 357

Fukugita, M., Ichikawa, T., Gunn, J. E., et al. 1996, AJ, 111, 1748

Gomes, R., Levison, H. F., Tsiganis, K., & Morbidelli, A. 2005, Nature, 435, 466

Jordi, C., Gebran, M., Carrasco, J. M., et al. 2010, A&A, 523, A48

Kaiser, N., Aussel, H., Burke, B. E., et al. 2002, in Society of Photo-Optical Instrumentation Engineers (SPIE) Conference Series, Vol. 4836, Proc. SPIE, ed. J. A. Tyson & S. Wolff, 154–164

Kochan, H. W., Huebner, W. F., & Sears, D. W. G. 1998, Earth Moon and Planets, 80, 369

Kolokolova, L., Hanner, M. S., Levasseur-Regourd, A. C., & Gustafson, B. Å. S. 2004, Physical properties of cometary dust from light scattering and thermal emission, ed. M. C. Festou, H. U. Keller, & H. A. Weaver, 577

Labrie, K., Anderson, K., Cárdenes, R., Simpson, C., & Turner, J. E. H. 2019, in Astronomical Society of the Pacific Conference Series, Vol. 523, Astronomical Data Analysis Software and Systems XXVII, ed. P. J. Teuben, M. W. Pound, B. A. Thomas, & E. M. Warner, 321

Levison, H. F., Morbidelli, A., Dones, L., et al. 2002, Science, 296, 2212

Lupton, R. 2005, Transformations between SDSS magnitudes and UBVRcIc, http://classic.sdss.org/dr4/algorithms/sdssUBVRITransform.html#Lupton2005, ,

Magnier, E. A., & Cuillandre, J. C. 2004, PASP, 116, 449

Magnier, E. A., Schlafly, E. F., Finkbeiner, D. P., et al. 2016a, arXiv e-prints, arXiv:1612.05242

—. 2016b, ArXiv e-prints, arXiv:1612.05242

Mainzer, A., Bauer, J., Grav, T., et al. 2011, ApJ, 731, 53

Mainzer, A., Bauer, J., Cutri, R. M., et al. 2014, ApJ, 792, 30

Meech, K. J., & Belton, M. J. S. 1990, AJ, 100, 1323

Meech, K. J., Buie, M. W., Samarasinha, N. H., Mueller, B. E. A., & Belton, M. J. S. 1997, AJ, 113, 844

Meech, K. J., Hainaut, O. R., Boehnhardt, H., & Delsanti, A. 2003, in AAS/Division for Planetary Sciences Meeting Abstracts #35, AAS/Division for Planetary Sciences Meeting Abstracts, 39.12

Meech, K. J., Jewitt, D., & Ricker, G. R. 1986, Icarus, 66, 561

Meech, K. J., & Raymond, S. N. 2020, Origin of Earth's water: Sources and constraints, ed. V. S. Meadows, G. V. Arney, B. E. Schmidt, & D. J. Des Marais, 325–353

Meech, K. J., & Weaver, H. A. 1996, Earth Moon and Planets, 72, 119

Meech, K. J., Yang, B., Kleyna, J., et al. 2016, Science Advances, 2, e1600038

Meech, K. J., Schambeau, C. A., Sorli, K., et al. 2017, AJ, 153, 206

Oort, J. H. 1950, BAN, 11, 91

Prialnik, D., Brosch, N., & Ianovici, D. 1995, MNRAS, 276, 1148

Raymond, S. N., & Izidoro, A. 2017, Icarus, 297, 134

Sarid, G., Prialnik, D., Meech, K. J., Pittichová, J., & Farnham, T. L. 2005, PASP, 117, 796

Tonry, J. L., Stubbs, C. W., Lykke, K. R., et al. 2012, ApJ, 750, 99

Tonry, J. L., Denneau, L., Heinze, A. N., et al. 2018a, PASP, 130, 064505

—. 2018b, PASP, 130, 064505

Tsiganis, K. 2015, Nature, 528, 202

Walsh, K. J., Morbidelli, A., Raymond, S. N., O'Brien, D. P., & Mandell, A. M. 2011, Nature, 475, 206

—. 2012, Meteoritics and Planetary Science, 47, 1941